Available online at www.sciencedirect.com
ScienceDirect
Trans. Nonferrous Met. Soc. China 34(2024) 2219−2230
Transactions of Nonferrous Metals Society of China
www.tnmsc.cn

Effects of aging on microstructure and wear resistance of laser cladding $Mo_{0.5}NbTiVCr_{0.25}$ high-entropy alloy coating

Ji HE[1,2,3], Hua-meng FU[1,3], Cui-rong LIU[2], Zheng-wang ZHU[1,3],
Long ZHANG[1,3], Zheng-kun LI[1,3], Hong LI[1,3], Hai-feng ZHANG[1,3]

1. CAS Key Laboratory of Nuclear Materials and Safety Assessment, Institute of Metal Research, Chinese Academy of Sciences, Shenyang 110016, China;
2. School of Science Materials and Technology, Taiyuan University of Science and Technology, Taiyuan 030024, China;
3. Shi-changxu Innovation Center for Advanced Materials, Institute of Metal Research, Chinese Academy of Sciences, Shenyang 110016, China

Received 15 November 2022; accepted 12 June 2023

Abstract: Refractory $Mo_{0.5}NbTiVCr_{0.25}$ high-entropy alloy coatings were fabricated on TC4 substrates using laser cladding technology. The coatings were aged at 600, 800 and 1000 °C for 24 h and then water-cooled. The phase composition, microstructure, and mechanical properties of the high-entropy alloy coatings were investigated using X-ray diffraction (XRD), scanning electron microscopy (SEM), electron backscattered diffraction (EBSD), transmission electron microscopy (TEM), Vickers hardness testing and universal friction wear testing. The results showed that high-entropy alloy coatings retained a body-centered cubic structure after different aging heat treatments. After the aging heat treatment at 800 °C, the coatings exhibited Ti-rich precipitation phases, which were verified as Ti(O,N) face-centered cubic structures by TEM technique. The optimum aging temperature was 600 °C and the hardness of the coating was $HV_{0.2}$ 410. The wear mechanisms of the coatings were adhesive and abrasive wear.
Key words: $Mo_{0.5}NbTiVCr_{0.25}$ alloy; laser cladding; refractory high-entropy alloy; microstructure; aging; wear

1 Introduction

In recent decades, safety has become a prerequisite for the successful use of nuclear technologies. Zirconium alloy cladding tubes are one of the most important components for maintaining fuel integrity and safety in nuclear power plants [1]. Approximately 70% of reactor fuel failure is caused by vibration-induced wear and penetration of external materials into the cladding [2]. Therefore, it is necessary to improve the structure and properties of Zr alloy cladding surfaces to extend their service life.

At present, laser cladding is a widely used surface modification technology that can not only improve the surface properties of damaged parts but also greatly reduce production costs and improve material utilization [3−5]. Additionally, the laser coatings exhibit fine microstructures, controllable metallurgical combinations, and low dilution rate [6]. They can significantly improve the wear resistance, corrosion resistance, heat resistance, oxidation resistance, and electrical properties of substrate material surfaces [7]. TANG et al [8] proposed surface-modified Zr cladding, and an outer

Corresponding author: Hua-meng FU, Tel: +86-13652419196, E-mail: hmfu@imr.ac.cn;
Hai-feng ZHANG, Tel: +86-13644016489, E-mail: hfzhang@imr.ac.cn
DOI: 10.1016/S1003-6326(24)66536-2

FeCrAl protective layer was selected as a coating to enhance the oxidative corrosion performance of laser-coated deposited Zr alloy. KHATKHATAY et al [9] deposited TiN and $Ti_{0.35}Al_{0.65}N$ coatings on Zr-4 substrates using pulsed laser deposition to improve the corrosion and wear resistances of the cladding layer.

Recently, iron-based alloys, Mo−Zr claddings, and SiC claddings have been used as coatings for zirconium alloy cladding tubes [10]. However, this study has some limitations. As a ceramic material, SiC can increase the surface hardness. However, the thermal expansion coefficient of the ceramic particles is too small, leading to a decrease in the oxidation resistance of the zirconium alloy cladding tubes. Moreover, some metal alloys do not have the ability to capture cross-sections with low neutrons and operate in high temperature water environments, which can easily lead to material cracking. Therefore, it is imperative to develop a versatile material to effectively improve its status.

The high-entropy alloy (HEA) exhibited outstanding characteristics such as high thermal stability, superior corrosion resistance, and resistance to radiation damage [11,12]. LI et al [13] conducted neutron irradiation experiments with NiFeCrMn HEAs, and the surface of this high-entropy alloy exhibited excellent radiation resistance. Generation IV nuclear reactors are expected to increase neutron flux and operate in the temperature range of 500−1300 K [14]. Zr-based (E110, E635, Zircaloys, M5, ZIRLO, etc.) claddings interact with water steam at a high temperatures (above 800 °C) [15], leading to embrittlement and oxidation problems through exothermic reactions. Laser cladding generates large residual stress, and heat treatment can reduce the residual stress inside the alloy and improve its mechanical properties. GUO et al [16] improved the mechanical properties of AlCoCrFeNi high-entropy alloys via heat treatment. Therefore, aging treatments at different temperatures were investigated in this study.

The preparation of refractory high-entropy alloy $Mo_{0.5}NbTiVCr_{0.25}$ coatings on TC4 substrates using laser cladding technology provides a novel research idea [17]. In this study, the effects of aging temperature on the microstructure and wear resistance of $Mo_{0.5}NbTiVCr_{0.25}$ HEA coatings were investigated. The aging temperatures were set at 600, 800, and 1000 °C, aging time was 24 h and water-cooling method was used. By characterizing the microstructure of the coating, the micro-structures at different locations of the coating at different aging temperatures also differed. In addition, the wear behavior and wear mechanism of the $Mo_{0.5}NbTiVCr_{0.25}$ HEA coating were systematically investigated.

2 Experimental

2.1 Substrate material

The substrate material used in this study was a traditional titanium alloy (Ti_6Al_4V, TC4) with dimensions of 150 mm × 80 mm × 30 mm. Chemical compositions of the alloy is listed in Table 1. To achieve better adhesion, the surface of the substrate was treated with emery paper ($120^{\#}$, $400^{\#}$, $800^{\#}$, and $1200^{\#}$) to remove dirt and rust, and then washed with anhydrous ethanol.

Table 1 Chemical composition of TC4 alloy (wt.%)

Fe	C	N	H
≤0.30	≤0.10	≤0.05	≤0.015
O	Al	V	Ti
≤0.20	5.5−6.8	3.5−4.5	Bal.

2.2 Alloy powder

In this study, the prealloyed $Mo_{0.5}NbTiVCr_{0.25}$ HEA powders were produced by the plasma atomization. The morphology of the powder was observed by scanning electron microscopy (SEM, Apreo−2C). As shown in Fig. 1(a), the HEA powders have a spherical and elliptical shape, which ensures the smoothness and continuity of the powder delivery during the test. The microstructure of the powder, observed under a microscope, was composed of dendritic crystals. Figure 1(b) shows the size distribution of the powders. The average diameter of the powders was measured to be 97 μm and the particle size distribution was from 84 to 150 μm. X-ray diffractometry (XRD, D8Advance) was used to characterize the phase compositions of the HEA powders. As shown in Fig. 1(c), the powder consists of a single BCC phase.

2.3 Laser cladding system

Laser cladding was carried out using a high-power fiber laser (YLS−4000-U-K, Germany) with

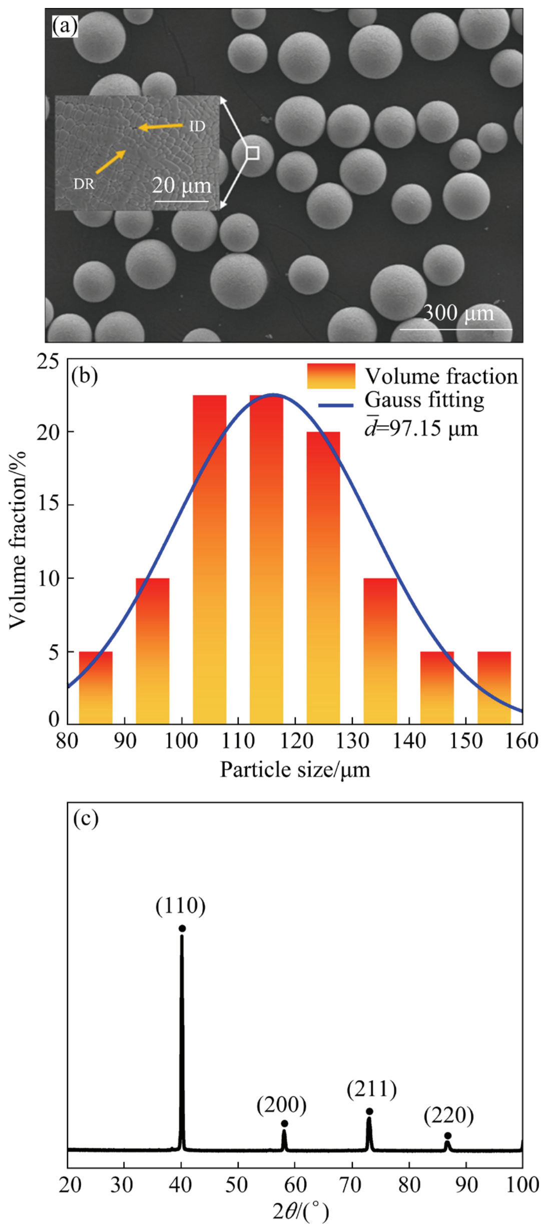

Fig. 1 SEM image (a), size distribution of spherical powders (b) and XRD pattern of HEA powders (c)

a coaxial power feeder machine. Figure 2 shows a schematic diagram of the laser cladding process. High-purity Ar protective gas was used to prevent the cladding material from being oxidized during the cladding process. The laser cladding process parameters are listed in Table 2. After laser cladding, the coating was vacuum sealed in a quartz tube and aged at 600, 800 and 1000 °C for 24 h, and finally cooled in water.

2.4 Microstructure characterization

Each coating was first treated with sandpaper, polished to a mirror shape using a slurry, and then ultrasonically cleaned with anhydrous ethanol. The coating was etched with an etching solution with HF/HNO_3 volume ratio of 1:3 for 10−15 s and then observed by microstructural analysis. The phase composition of the sprayed and aged coatings was identified by X-ray diffractometry (XRD, D8Advance) with Cu K_α radiation and a scan range of 2θ=20°−100°. The microstructure of the coating was characterized by scanning electron microscopy (SEM, Thermo-scientific-Apreo−2C). The cross-sectional microstructure of the coating was observed by electron backscattered diffraction (EBSD; MIRA3-OXFORD). The microstructure of the coatings was observed using transmission electron microscopy (TEM, Tecnai-F20).

2.5 Microhardness and tribological behavior tests

The hardness test equipment for the cross-sectional samples under different treatment conditions was a KB30SRFA micro-Vickers hardness tester. The load was 0.2 kg, the loading time was 6 s, and the holding time was 15 s. The top of the HEA coating along the longitudinal section was taken every 200 μm and measured until the substrate hardness was constant. Prior to the friction and wear experiments, the samples were ground, polished to a mirror effect, and cleaned with ethanol. Friction and wear experiments were performed at room temperature using a universal wear tester (UMT−2) with small Si_3N_4 balls with a diameter of 3 mm. The load was 5 N, the frequency was 1 Hz, and the wear length was 10 mm. A 30 min reciprocating dry friction experiment was conducted.

3 Results and discussion

3.1 XRD patterns

Figure 3 shows the XRD patterns of the as-sprayed and aged HEA coatings. The results indicate that both the clad- and heat-treated coatings exhibited a BCC solid solution phase without the formation of other phases. This indicates that $Mo_{0.5}NbTiVCr_{0.25}$ HEA has high thermal stability. Considering the strongest peak of Bragg's law, the (110) peak exhibits the strongest intensity among all the peaks under all conditions, indicating that the crystal along this parallel direction preferentially grows. No Ti-rich phase was found in the XRD characterization, but the Ti-rich phase was observed

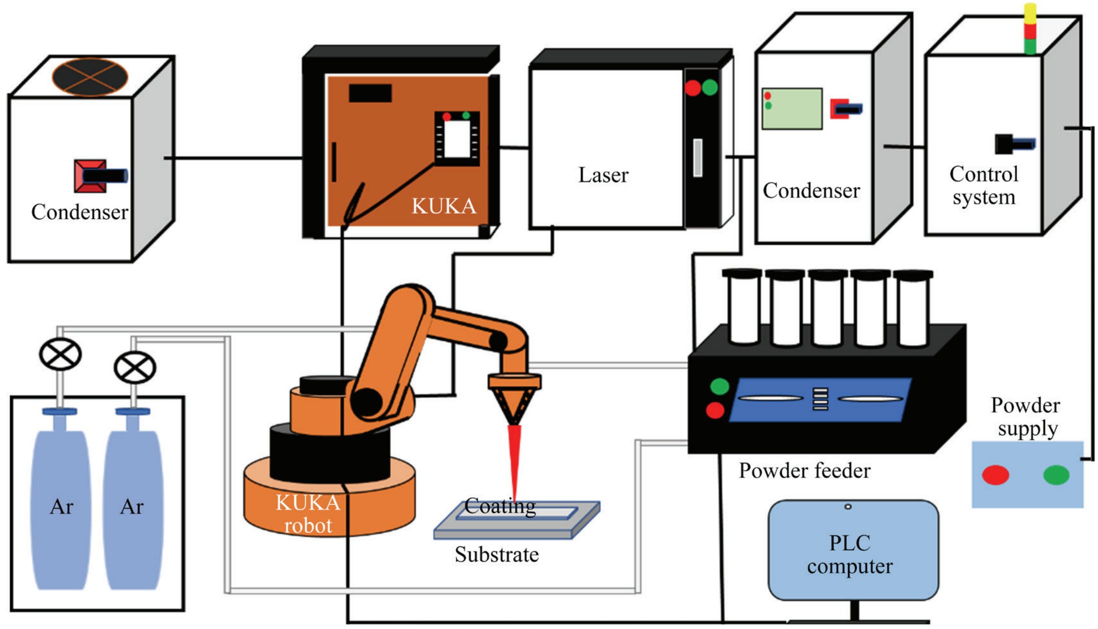

Fig. 2 Schematic diagram of laser cladding process

Table 2 Experimental parameters of laser cladding HEAs coating

Laser power/W	Scanning speed/ $(mm \cdot s^{-1})$	Spot diameter/ mm	Defocus amount/ mm	Overlap/ %
1600	8	5	17	50

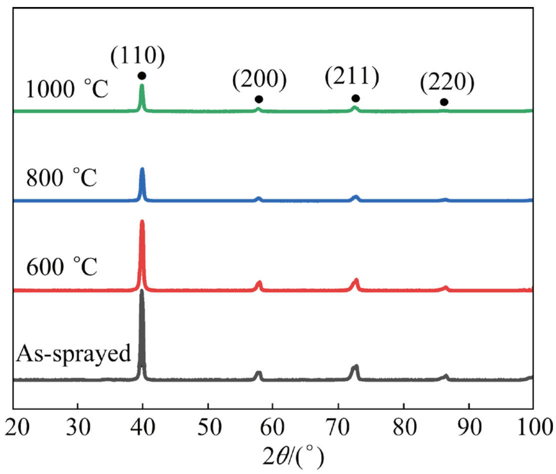

Fig. 3 XRD patterns of as-sprayed and aged $Mo_{0.5}NbTiVCr_{0.25}$ HEA coatings at different temperatures

in the SEM at 800 and 1000 °C (Fig. 4). This may be because the crystals are too small and beyond the spatial resolution of the XRD.

3.2 SEM images

Figure 4 shows SEM images of the HEA coatings at different locations and different aging temperatures. Because of the nature of laser melting, the microstructure is affected by the temperature gradient and cooling rate, and the microstructure displays different structures. In Fig. 4, the top and middle of the coating were dominated by the dendritic crystal structure, and the bottom of the coating was dominated by columnar and cellular crystals. The coating had certain defects such as pores. As shown in Figs. 4(h) and (j), the coating had a small amount of Ti-rich phase after the aging heat treatment at 800 °C and 1000 °C, respectively, which was not detected in XRD. In Figs. 4(j−l), the diffusion between elements was more obvious after the coating was aged at 1000 °C. The microstructures of the coatings at different positions were not evident, and there was a clear tendency for dendritic growth.

In Fig. 5(a), the EDS surface scan distribution of the high-entropy alloy coating under aging treatment at 800 °C is shown. There are a small number of Ti-rich phase and Cr precipitates in the coating. Ti primarily precipitates between the dendrites, and a small amount of Cr is dispersed at different positions. Mo and Nb are distributed in the dendrites, whereas Ti, Cr, and V are distributed in the interdendrites. As shown in Fig. 5(c), this elemental segregation is caused by the melting point difference between the elements and the mixing enthalpy between the atomic pairs. During the non-equilibrium solidification of the alloy, the dendritic phase containing high-melting point elements

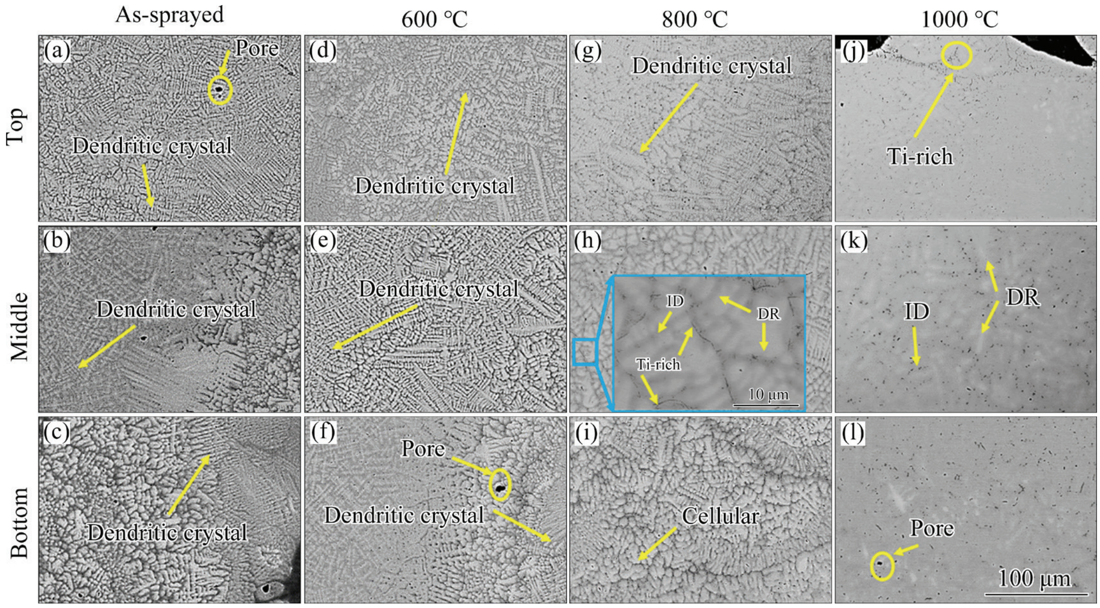

Fig. 4 SEM images of $Mo_{0.5}NbTiVCr_{0.25}$ HEA coatings processed at different aging temperatures and different locations: (a−c) As-sprayed; (d−f) 600 °C; (g−i) 800 °C; (j−l) 1000 °C

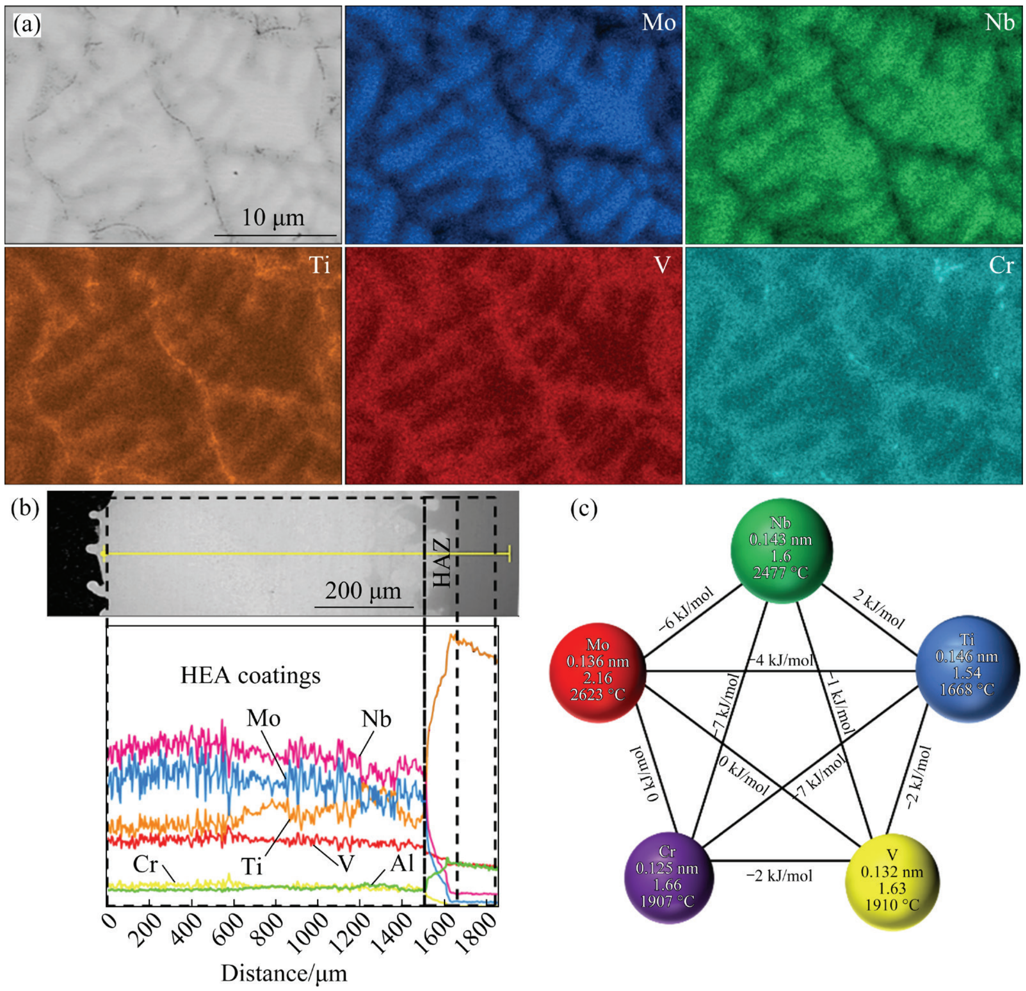

Fig. 5 EDS simultaneous surface scan distribution of $Mo_{0.5}NbTiVCr_{0.25}$ HEA coating aged at 800 °C (a), EDS simultaneous line scan distribution of as-sprayed coatings (b) and enthalpy of mixing between different atomic pairs, atomic radius, electronegativity, and melting point (c)

precipitates from the liquid phase first, and the interdendritic phase containing low-melting point elements precipitates later. Therefore, Ti, V, and Cr precipitate out of the interdendritic phase and undergo elemental segregation. This phenomenon has often been observed in HEA, such as Al_xHfNbTaTiZr [18], HfMo_xNbTaTiZr [19], and Cr$Mo_{0.5}$Nb$Ta_{0.5}$TiZr [20] alloys, consisting of alloying elements with widely varying melting points.

Figure 5(b) shows the line scan distribution of the high-entropy alloy coating without heat treatment. From the line scan distribution in Fig. 5, we can see a clear division between the high-entropy alloy coatings, heat-affected zone (HAZ), and the substrate. As shown in Fig. 5(b), a small amount of Al in the substrate penetrates the high-entropy alloy coating, whereas no Al-related phase is detected in the XRD pattern of Fig. 3; therefore, it can be determined that only a small amount of Al penetrates the coating. In Fig. 5(b), the curve exhibits a fluctuating trend, indicating that the elements in the coating exhibit a certain deviation, which corresponds to the phenomenon shown in Fig. 5(a).

3.3 TEM images

To further analyze the detailed microstructure of the Ti-rich dark phase, we analyzed the coating aged at 800 °C by transmission electron microscopy. Figure 6(a) shows a bright-field (BF) TEM image and selective area diffraction (SAD) pattern of the high-entropy alloy coating. According to the SAD model, two different phases can be identified in the coating: BCC and FCC. Combined with the elemental maps in Fig. 6(b), a Ti-rich FCC precipitate was produced, which may have been formed by contact with air containing C, N, and O to form Ti(C,N,O). XIANG et al [21] reported that a TiO phase with an FCC structure was formed in an NbMoTaWVTi refractory HEA owing to the introduction of O during the preparation process. In addition, ZHANG et al [22] reported a TiC phase with an FCC structure in an NbMoCrTiAl HEA. In this study, an HEA coating was prepared by aging heat treatment after laser melting. The formation of the Ti-rich FCC structure was attributed to the adsorption of C, N, and O during the preparation process.

Based on the SAD pattern of the precipitated phase shown in Fig. 6, the lattice parameter of the Ti-rich FCC phase was determined to be 0.4204 nm. The lattice constants of TiO, TiC, and TiN are 0.4177, 0.4327, and 0.4244 nm, respectively [21]. Based on the above discussion, the Ti-rich precipitates aged at 800 and 1000 °C may be Ti(O,N) phase with FCC structure.

3.4 EBSD analysis results

Figure 7 shows the IPF, KAM, and grain size distribution of the HEA coatings at different aging temperatures. The IPF diagram of the construction direction (BD) shows an alternating distribution of large particles and fine equiaxed grains. This grain size distribution was mainly caused by multitrack laser scanning, and remelting, reheating, and rapid cooling occurred repeatedly during the multitrack process. The crystal growth direction in the IPF shown in Fig. 7 was not uniform, and there was no

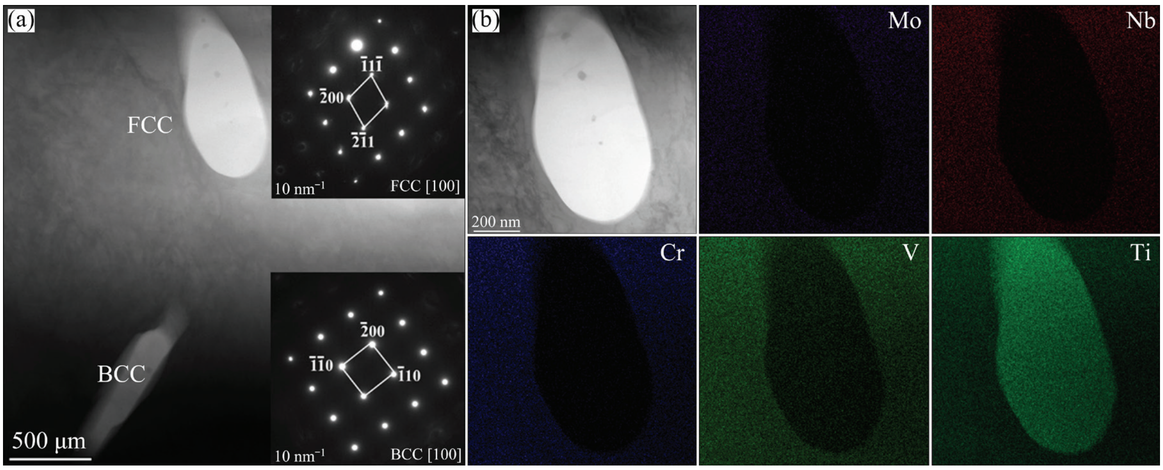

Fig. 6 BF TEM image (a) and elemental mappings of Mo, Nb, Cr, V and Ti (b) for $Mo_{0.5}$NbTiV$Cr_{0.25}$ HEA coatings after aging at 800 °C

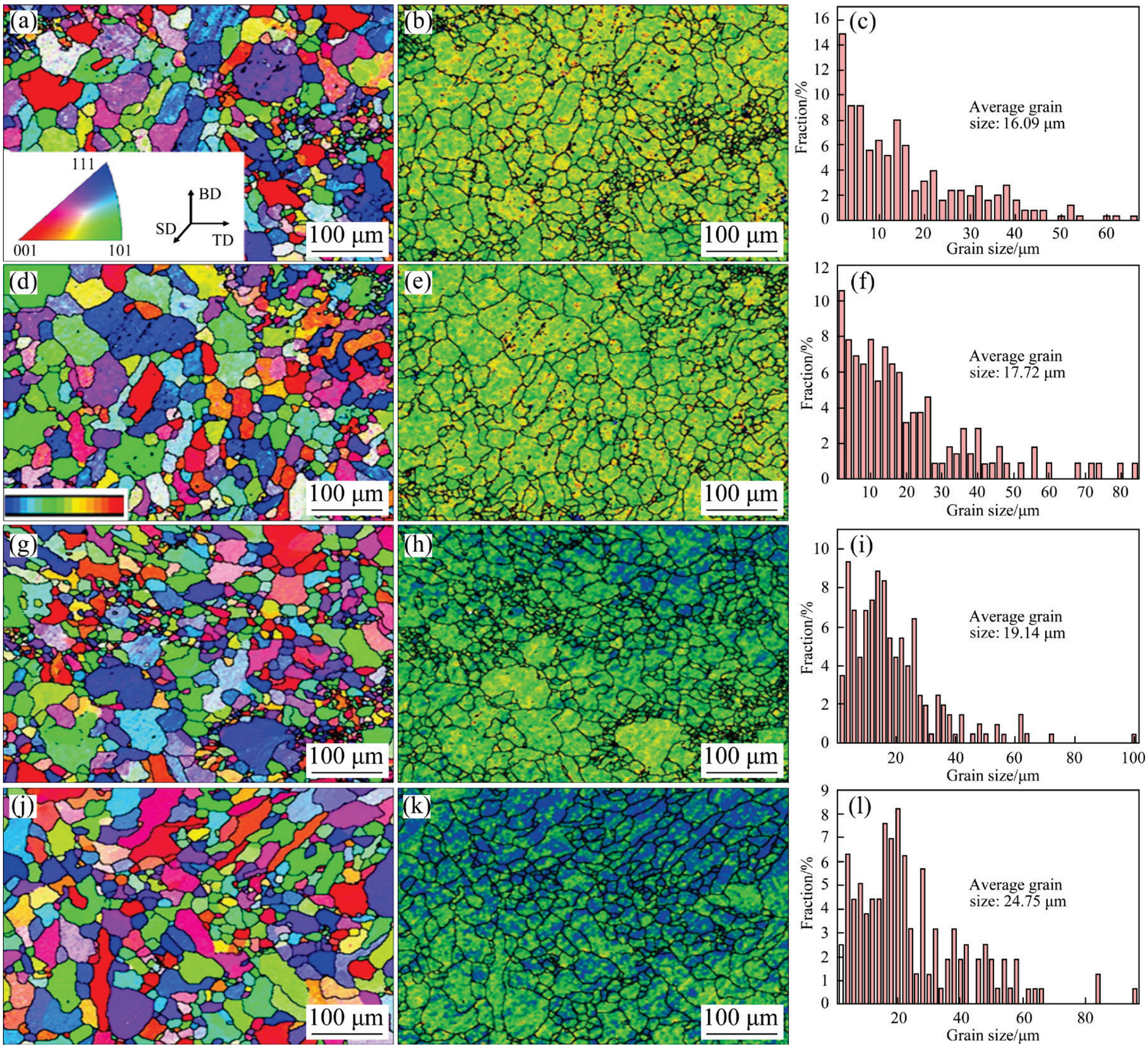

Fig. 7 IPF (a, d, g, j), KAM (b, e, h, k) diagrams and grain size distribution (c, f, i, l) of HEA coatings at different aging temperatures: (a−c) As-sprayed; (d−f) 600 °C; (g−i) 800 °C; (j−l) 1000 °C

clear direction of crystal growth. According to the grain size statistics (Figs. 7(c, f, i, l)), the grain size of the coating increased with the increase in aging temperature after treatment. The average grain size was between 16.09 and 24.75 μm, but the size change was not significant. According to ZHANG et al [22] for 300M steel, the average size of the precipitates after heat treatment (d) can be expressed by the reconstructed Arrhenius-type equation as follows:

$$d = At^n \exp\left(-\frac{Q}{RT}\right) \tag{1}$$

where Q is the activation energy for precipitate growth, T is the heating temperature, t is the holding time, R is the molar gas constant (8.314 J/(mol·K)), and A and n are constants for the given material. According to this equation, as the aging temperature increases, the driving force for the nucleation and growth of precipitates increases, which leads to an increase in the grain size and volume fraction.

In the KAM diagrams in Figs. 7(b, e, h, k), there is some residual stress when the coating is not heat-treated. As the aging temperature increases, the residual stress in the coating gradually decreases. In Figs. 7(h, k), there is almost no residual stress inside the coating after aging treatment at 800 and 1000 °C. In the KAM diagram, green approximation indicates the presence of dislocations. This is due to the rapid cooling and heating characteristics of the laser cladding, resulting in many dislocations in the cladding layer. The dislocations in Figs. 7(b, e, h, k) mainly exist inside and near the grain boundaries. Similarly, the color in the KAM diagram reflects the size of the Schmidt coefficient. Yellow represents a relatively low Schmidt coefficient and red represents a relatively high Schmidt coefficient, which indirectly determines the quality characteristics of the material.

3.5 Microhardness of coatings

Figure 8 shows the microhardness of the coating, average hardness at different positions after aging, and cross-section morphology of the coatings. As shown in Figs. 8(a) and (c), the micro-hardness of the coating after the aging treatment was greater than that of the HAZ and the substrate. Combined with the average hardness of the coating at different aging temperatures in Fig. 8(b), the best aging hardening occurs at 600 °C, and the aging heat treatment is $HV_{0.2}$ 410. However, the hardening effect decreases with increasing temperature. This is mainly due to the decrease in hardness caused by the reduction and recrystallization of the coating during the aging process. Combined with the EBSD analysis in Fig. 7, the increase in grain size leads to a decrease in dislocation density, which causes a decrease in microhardness. At the same time, when the coating was heat-treated at 800 °C, the FCC precipitated phase containing Ti appeared, resulting in a decrease in the hardness of the coating. Even at an aging temperature of 1000 °C, the coating did not show obvious softening phenomenon. The coating exhibited good softening resistance and may be ideal for irradiation-resistant nuclear materials [23].

This phenomenon can be explained by the changes in the XRD pattern of the HEA coating after aging. The (110) peak of the BCC phase of this high-entropy alloy coating shifted to a lower angle, indicating a strong lattice distortion. Therefore, the BCC solid solution annealed at 600 °C has a higher solid solution strengthening effect, thus increasing the microhardness of the coating.

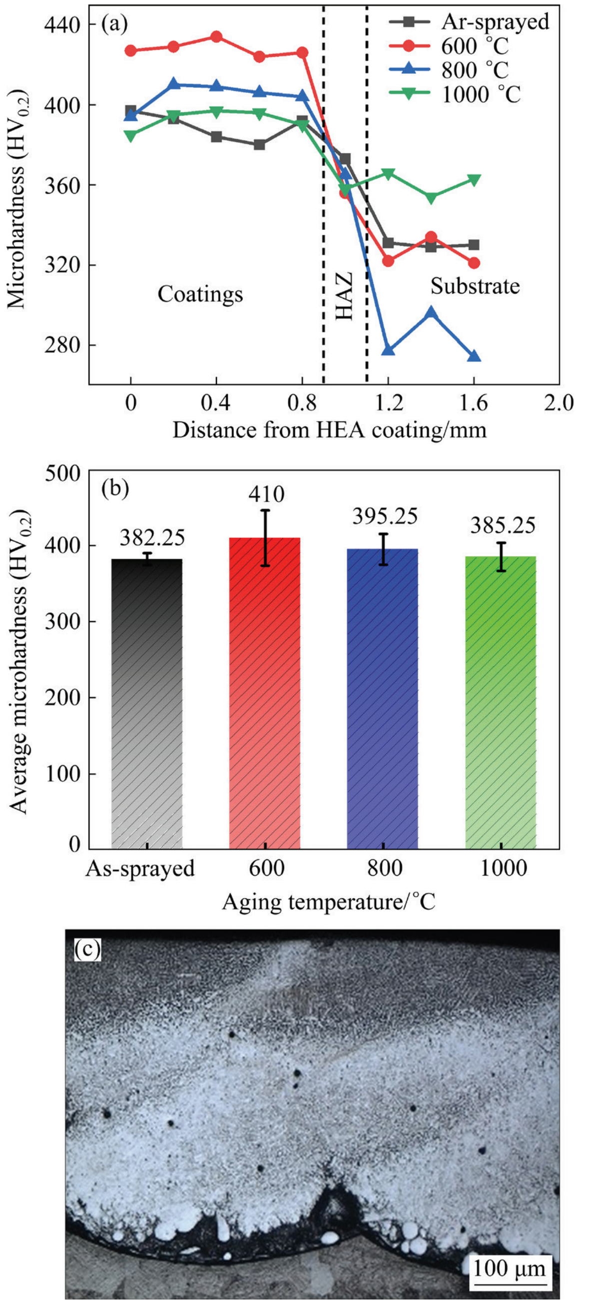

Fig. 8 Microhardness and cross-section morphology of HEA coatings: (a) Microhardness at different distances from HEA coating; (b) Average microhardness of coating after aging; (c) Cross-section morphology of HEA coating

3.6 Friction properties of coatings

Figure 9(a) shows the friction coefficients of $Mo_{0.5}NbTiVCr_{0.25}$ HEA coatings aged at different temperatures. The overall friction coefficient of the coating fluctuated considerably between 0.6 and 0.8. The sawtooth behavior of the friction coefficient fluctuation curve is influenced by the grain orientation, grain size, and composition deviation [24]. According to Arca's law [25], the friction coefficient of wear-resistant materials is inversely proportional to their hardness. Figure 9(b) shows the wear loss of the $Mo_{0.5}NbTiVCr_{0.25}$ HEA coating at different aging temperatures. The wear mass values of the high-entropy alloy coating at different aging states were in the range of 0.41−0.56 mg. There was no significant difference in the wear mass of the high-entropy alloy coating, indicating that the high-entropy alloy had good wear resistance.

Figure 10 shows the SEM images revealing the wear morphology of the high-entropy alloy coating under different aging conditions. The wear surface has slight grooving and fine delamination, as well as some coating debris. The coating exhibits extensive scratches, spalling, and plastic deformation along the sliding direction. Coating with a lower micro-hardness leads to more plastic deformation. A large amount of frictional heat tends to accumulate on the contact surface, leading to adhesive wear [26]. As shown in Fig. 10, the wear pattern of the coating is mainly caused by adhesive and abrasive wear.

The experimental results were analyzed using the surface energy mechanism. The friction coefficient was affected by the adhesion forces of the two friction surfaces. The higher the friction force, the higher the friction coefficient. The adhesive force is expressed in terms of the adhesive surface energy (W_{ab}) [27]. The expression is as follows:

$$W_{ab}=\gamma_a+\gamma_b+\gamma_{ab} \tag{2}$$

where γ_a is the surface free energy per unit area of the coating, γ_b is the surface free energy per unit area of the corresponding ball, γ_{ab} is the interaction energy between the two friction pairs. An increase in temperature at any time and the growth of the grain size reduce the energy at the interface. Therefore, γ_a decreases, leading to a decrease in W_{ab}. According to recent findings [28], surface energy is

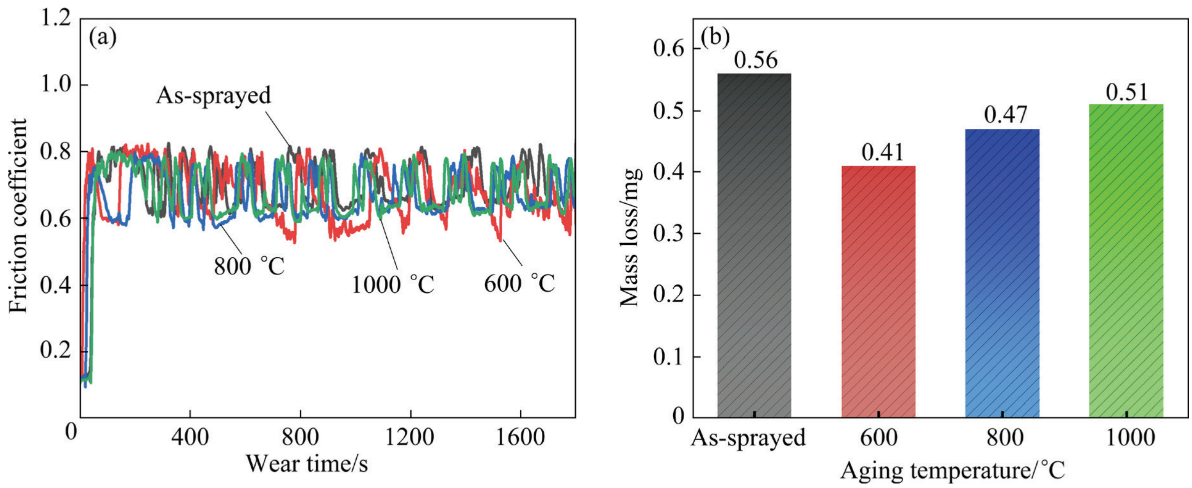

Fig. 9 Friction coefficient (a) and wear loss (b) of $Mo_{0.5}NbTiVCr_{0.25}$ HEA coatings at different aging temperatures

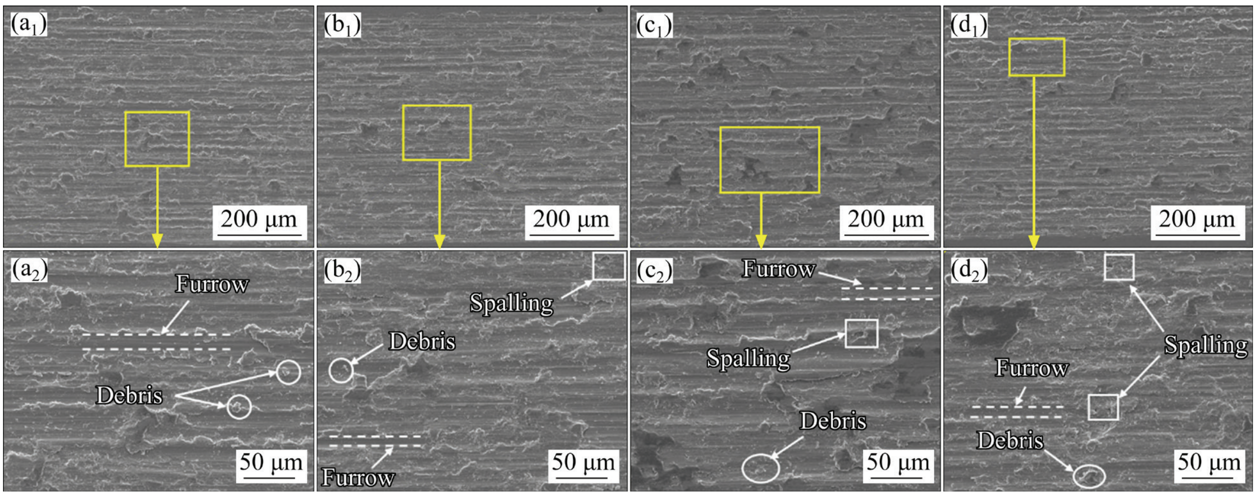

Fig. 10 SEM images of wear morphology of HEA coatings under different aging conditions: (a_1, a_2) As sprayed; (b_1, b_2) 600 °C; (c_1, c_2) 800 °C; (d_1, d_2) 1000 °C

only a part of the friction energy, and most of it is consumed during the elastic and plastic deformation of the metal.

Stress concentration is an important factor for coating spalling, which is caused by microstructural inhomogeneity due to the rapid solidification characteristics of the laser cladding. Aging heat treatment can reduce the influence of the residual stress and improve the wear resistance of the coating. However, combined with the above hardness analysis, 600 °C is the best aging temperature, so the wear loss is the lowest. Experience has proven that the microhardness of the coating is the main factor that reduces the wear rate. Therefore, an increase in hardness leads to an improvement in the wear resistance of the coating.

4 Conclusions

(1) According to XRD analysis, the crystal structure of the high-entropy alloy coating remained a BCC structure after aging heat treatment at 600, 800, and 1000 °C, indicating that the high-entropy alloy coating had a good thermal stability.

(2) The aged and coated high-entropy alloy coatings exhibited dendritic structures. There were two phases in the samples aged at 800 and 1000 °C, including BCC structure and a small amount of Ti-rich FCC structure precipitates. The FCC phase is rich in Ti because of the absorption of oxygen and nitrogen during the preparation process. Therefore, the Ti-rich FCC phase is proposed to be Ti(O,N).

(3) As the aging heat treatment temperature increased, the coating hardness became higher than that of the molten state, which was an aging hardening effect. Moreover, 600 °C was the optimum aging temperature with the coating hardness of $HV_{0.2}$ 410.

(4) The main wear mechanisms of the high-entropy alloy coating were adhesive and abrasive. The wear of the coatings ranged from 0.41 to 0.56 mg. With the increase in aging temperature, the least wear was observed at the aging heat treatment of 600 °C, where the wear loss mass of the coating was 0.41 mg. The friction coefficient of the high-entropy alloy coating remained between 0.6 and 0.8, indicating that this high-entropy alloy had good resistance to softening.

CRediT authorship contribution statement

Ji HE: Conceptualization, Date curation, Formal analysis, Investigation, Software, Writing − Original draft, Writing − Review & editing; **Hua-meng FU:** Conceptualization, Funding acquisition, Project administration, Supervision, Writing − Review & editing; **Cui-rong LIU:** Methodology, Supervision; **Zheng-wang ZHU:** Visualization, Writing – Review & editing; **Long ZHANG:** Data curation, Software; **Zheng-kun LI:** Resources, Supervision; **Hong LI:** Visualization, Project administration; **Hai-feng ZHANG:** Methodology, Writing − Review & editing.

Declaration of competing interest

The authors declare that they have no known competing financial interests or personal relationships that could have appeared to influence the work reported in this paper.

Acknowledgments

This work was supported by the National Key Research and Development Program (No. 2021YFA0716303), Chinese Academy of Sciences of China (No. ZDBS-LY-JSC023), and Ling-Chuang Research Project of the China National Nuclear Corporation.

References

[1] MOTTA A T, CAPOLUNGO L, CHEN L Q, CINBIZ M N, DAYMOND M R, KOSS D A, LACROIX E, PASTORE G, SIMON P C A, TONKS M R, WIRTH B D, ZIKRY M A. Hydrogen in zirconium alloys: A review [J]. Journal of Nuclear Materials, 2019, 518: 440−460.

[2] ALLEN T, BUSBY J, MEYER M, PETTI D. Materials challenges for nuclear systems [J]. Materials Today, 2010, 13: 14−23.

[3] LI Rui-di, NIU Peng-da, YUAN Tie-chui, LI Zhi-ming. Displacive transformation as pathway to prevent micro-cracks induced by thermal stress in additively manufactured strong and ductile high-entropy alloys [J]. Transactions of Nonferrous Metals Society of China, 2021, 31: 1059−1073.

[4] CHEN Tao, WU Wei-ning, LI Wen-peng, LIU De-fu. Laser cladding of nanoparticle TiC ceramic powder: Effects of process parameters on the quality characteristics of the coatings and its prediction model [J]. Optics & Laser Technology, 2019, 116: 345−355.

[5] ZHANG Ying, HAN Teng-fei, XIAO Meng, SHEN Yi-fu. Effect of process parameters on the microstructure and properties of laser-clad $FeNiCoCrTi_{0.5}$ high-entropy alloy coating [J]. International Journal of Minerals, Metallurgy and Materials, 2020, 27: 630−639.

[6] MA Min-yu, XIONG Wen-jing, LIAN Yong, HAN Dong,

ZHAO Chao, ZHANG Jin. Modeling and optimization for laser cladding via multi-objective quantum-behaved particle swarm optimization algorithm [J]. Surface and Coatings Technology, 2021, 381: 125129.

[7] ZENG Chao, TIAN Wei, LIAO Wen-he, HUA Liang. Microstructure and porosity evaluation in laser-cladding deposited Ni-based coatings [J]. Surface and Coatings Technology, 2016, 294: 122−130.

[8] TANG C C, STUEBER M, SEIFERT H J, STEINBRUECK M. Protective coatings on zirconium-based alloys as accident-tolerant fuel (ATF) claddings [J]. Corrosion Reviews, 2017, 35: 141−165.

[9] KHATKHATAY F, JIAO Liang, JIAN Jie, ZHANG Wen-rui, JIAO Zhi-jie, GAN Jian, ZHANG Hong-bin, ZHANG Xing-hang, WANG Hai-yan. Superior corrosion resistance properties of TiN-based coatings on Zircaloy tubes in supercritical water [J]. Journal of Nuclear Materials, 2014, 451: 346−351.

[10] KIM H G, KIM I H, JUNG Y I, PARK D J, PARK J Y, KOO Y H. Adhesion property and high-temperature oxidation behavior of Cr-coated Zircaloy-4 cladding tube prepared by 3D laser coating [J]. Journal of Nuclear Materials, 2015, 465: 531−539.

[11] WANG Wen-chang, LI Jia-xing, GE Yuan, KONG De-jun. Structural characteristics and high-temperature tribological behaviors of laser cladded NiCoCrAlY−B_4C composite coatings on Ti6Al4V alloy [J]. Transactions of Nonferrous Metals Society of China, 2021, 31: 2729−2739.

[12] ZENG Min, YAN Hong, YU Bao-biao, HU Zhi. Microstructure, microhardness and corrosion resistance of laser cladding Ni−WC coating on $AlSi_5Cu_1Mg$ alloy [J]. Transactions of Nonferrous Metals Society of China, 2021, 31: 2716−2728.

[13] LI Cong-yi, HU Xun-xiang, YANG Teng-fei, KUMAR N A P K, WIRTH B D, ZINKLE S J. Neutron irradiation response of a Co-free high entropy alloy [J]. Journal of Nuclear Materials, 2019, 527: 151838.

[14] OLSON G B. Genomic materials design: The ferrous frontier [J]. Acta Materialia, 2013, 61: 771−781.

[15] KASHKAROV E, AFORNU B, SIDELEV D, KRINITCYN M, GOUWS V, LIDER A. Recent advances in protective coatings for accident tolerant Zr-based fuel claddings [J]. Coatings, 2021, 11: 557.

[16] GUO Wei-min, DING Ning, LIU Guo-qiang, JING Cai-nian, XU Hui-xia, LIU Long, XU Na, WU Xiao-feng, HE Jian-qun, ZAIRI F. Microstructure evolution of a multi-track AlCoCrFeNi high entropy alloy coating fabricated by laser cladding [J]. Materials Characterization, 2022, 184: 111660.

[17] LIU Rui-ping, XU Ting-ting, WANG Chang-an. A review of fabrication strategies and applications of porous ceramics prepared by freeze-casting method [J]. Ceramics International, 2016, 42: 2907−2925.

[18] LIN C M, JUAN C C, CHANG C H, TSAI C W, YEH J W. Effect of Al addition on mechanical properties and microstructure of refractory $Al_xHfNbTaTiZr$ alloys [J]. Journal of Alloys and Compounds, 2015, 624: 100−107.

[19] JUAN C C, TSENG K K, HSU W L, TSAI M H, TSAI C W, LIN C M, CHEN S K, LIN S J, YEH J W. Solution strengthening of ductile refractory $HfMo_xNbTaTiZr$ high-entropy alloys [J]. Materials Letters, 2016, 175: 284−287.

[20] LI Tian-chen, LIU Bin, LIU Yong, GUO Wen-min, FU Ao, LI Liang-sheng, YAN Nie, FANG Qi-hong. Microstructure and mechanical properties of particulate reinforced NbMoCrTiAl high entropy based composite [J]. Entropy (Basel), 2018, 20: 517.

[21] XIANG Chao, FU Hua-meng, ZHANG Zhi-ming, HAN En-hou, ZHANG Hai-feng. Effect of Cr content on microstructure and properties of $Mo_{0.5}VNbTiCr_x$ high-entropy alloys [J]. Journal of Alloys and Compounds, 2020, 818: 153352.

[22] ZHANG S S, LI M Q, LIU Y G, LUO J, LIU T Q. The growth behavior of austenite grain in the heating process of 300M steel [J]. Materials Science and Engineering A, 2011, 528: 4967−4972.

[23] GUO Ya-xiong, LIU Qi-bin, SHANG Xiao-juan. Investigation on annealing strengthening effect of laser cladding $Fe_5Cr_5Co_5SiTiNbMoW$ high-entropy alloy coating [J]. Journal of Materials Research, 2018, 33: 3339−3346.

[24] LI Xiao-feng, FENG Ying-hao, LIU Bin, YI Deng-hao, YANG Xiao-hui, ZHANG Wei-dong, CHEN Gang, LIU Yong, BAI Pei-kang. Influence of NbC particles on microstructure and mechanical properties of AlCoCrFeNi high-entropy alloy coatings prepared by laser cladding [J]. Journal of Alloys and Compounds, 2019, 788: 485−494.

[25] ARCHARD J F. Contact and rubbing of flat surfaces [J]. Journal of Applied Physics, 1953, 24: 981−988.

[26] DIMAKI A V, DUDKIN I V, POPOV V L, SHILKO E V. Influence of the adhesion force and strain hardening coefficient of the material on the rate of adhesive wear in a dry tangential frictional contact [J]. Russian Physics Journal, 2019, 62: 1398−1408.

[27] JIAO Xiang-yi, WANG Can-ming, GONG Zheng-qi, WANG Gui-ming, SUN Hong-fei, YANG Hong-ru. Effect of Ti on T15M composite coating fabricated by laser cladding technology [J]. Surface and Coatings Technology, 2017, 325: 643−649.

[28] ZHANG Da-wei, OU Heng-an. Relationship between friction parameters in a Coulomb–Tresca friction model for bulk metal forming [J]. Tribology International, 2016, 95: 13−18.

时效处理对激光熔覆 $Mo_{0.5}NbTiVCr_{0.25}$ 高熵合金涂层显微组织和耐磨性能的影响

何 吉[1,2,3]，付华萌[1,3]，刘翠容[2]，朱正旺[1,3]，张 龙[1,3]，李正坤[1,3]，李 宏[1,3]，张海峰[1,3]

1. 中国科学院 金属研究所 核材料与安全评价重点实验室，沈阳 110016；
2. 太原科技大学 材料科学与工程学院，太原 030024；
3. 中国科学院 金属研究所 师昌绪先进材料创新中心，沈阳 110016

摘 要：通过激光熔覆技术在 TC4 基体上制备难熔 $Mo_{0.5}NbTiVCr_{0.25}$ 高熵合金涂层。涂层在 600、800 和 1000 ℃下时效热处理 24 h，然后水冷。采用 X 射线衍射(XRD)、扫描电子显微镜(SEM)、电子背散射衍射(EBSD)、透射电子显微镜(TEM)等技术、以及维氏硬度和万能摩擦磨损测试手段对高熵合金涂层的相组成、显微组织和力学性能进行研究。结果表明，高熵合金涂层经不同时效热处理后仍保持体心立方结构。经 800 ℃时效热处理后，涂层含有富 Ti 沉淀相，通过 TEM 术证实其为 Ti(O,N)面心立方结构。最佳时效温度为 600 ℃，涂层硬度为 $HV_{0.2}$ 410。该涂层的磨损机制为黏着磨损和磨料磨损。

关键词：$Mo_{0.5}NbTiVCr_{0.25}$ 合金；激光熔覆；难熔高熵合金；显微组织；时效；磨损

(Edited by Wei-ping CHEN)